Title

Meridional volume transport in the South Pacific: Mean and SAM-related variability

Permalink

https://escholarship.org/uc/item/2927d8qp

Journal

Journal of Geophysical Research - Oceans, 119(4)

ISSN

2169-9275

Authors

Zilberman, NV
Roemmich, DH
Gille, ST

Publication Date

2014-04-01

DOI

10.1002/2013jc009688

AGU PUBLICATIONS

JGR

Journal of Geophysical Research: Oceans

RESEARCH ARTICLE

10.1002/2013JC009688

Special Section:

Western Pacific Ocean Circulation and Climate

Key Points:

- Improved meridional volume transport in the South Pacific using Argo
- EAC transport variability tied to the SAM

Correspondence to:

N. V. Zilberman,
nzilberman@ucsd.edu

Citation:

Zilberman, N. V., D. H. Roemmich, and S. T. Gille (2014), Meridional volume transport in the South Pacific: Mean and SAM-related variability, *J. Geophys. Res. Oceans*, *119*, 2658–2678, doi:10.1002/2013JC009688.

Received 9 DEC 2013
Accepted 24 MAR 2014
Accepted article online 28 MAR 2014
Published online 25 APR 2014

Meridional volume transport in the South Pacific: Mean and SAM-related variability

N. V. Zilberman[1], D. H. Roemmich[1], and S. T. Gille[1]

[1]Scripps Institution of Oceanography, University of California San Diego, La Jolla, California, USA

Abstract The large increase in upper-ocean sampling during the past decade enables improved estimation of the mean meridional volume transport in the midlatitude South Pacific, and hence of the climatically important Meridional Overturning Circulation. Transport is computed using Argo float profile data for geostrophic shear and trajectory data for reference velocities at 1000 m. For the period 2004–2012, the mean geostrophic transport across 32°S is 20.6 ± 6.0 Sv in the top 2000 m of the ocean. From west to east, this includes the southward East Australian Current (23.3 ± 2.9 Sv), its northward recirculation (16.3 ± 3.6 Sv), the broad interior northward flow (18.4 ± 4.1 Sv), and the net northward flow (9.2 ± 2.2 Sv) in opposing currents in the eastern Pacific. The basin-integrated geostrophic transport includes 7.3 ± 0.9 Sv of surface and thermocline waters, 4.9 ± 1.0 Sv of Subantarctic Mode Water, and 4.9 ± 1.4 Sv of Antarctic Intermediate Water. Interannual variability in volume transport across 32°S in the South Pacific shows a Southern Annual Mode signature characterized by an increase during the positive phase of the Southern Annular Mode and a decrease during the negative phase. Maximum amplitudes in geostrophic transport anomalies, seen in the East Australian Current and East Australian Current recirculation, are consistent with wind stress curl anomalies near the western boundary.

1. Introduction

The mass, heat, and freshwater transported by the mean ocean circulation are central to the oceanic contribution to the climate system. The energy and water cycle involves northward heat transport in the Atlantic, poleward heat transport in the combined Indo-Pacific, and freshwater transports directed away from the excess rainfall regions of the tropics, and high latitudes toward the evaporative subtropics [*Talley*, 2003, 2008]. The oceanic mass transport is partitioned vertically into shallow meridional overturning circulation cells running across the equator in the Atlantic and the Indian Oceans and at mid to low latitudes in the Pacific, and deep cross-equatorial cells below [*Ganachaud and Wunsch*, 2003; *Macdonald et al*., 2009]. On a global scale, mean oceanic transports of heat and freshwater are expected to balance surface fluxes of heat and freshwater, maintaining a quasi-steady state.

The World Ocean Circulation Experiment (WOCE) of the 1990s included an ensemble of zonal and meridional top-to-bottom vertical hydrographic sections covering most ocean basins. One of the principal objectives in designing the WOCE field program was to make direct estimates of the meridional mass transport, and of the transfer of heat and fresh water in the global ocean. A sampling strategy was for meridional transport at about 30° north and south in each ocean basin to be inferred from a set of coast-to-coast zonal sections and western boundary current (WBC) moored arrays at those midsubtropical gyre latitudes. Unfortunately, the sparsity of the WOCE sections in space and time generated large uncertainties in the transport estimates and hindered accurate assessment of ocean variability [*Ganachaud and Wunsch*, 2003; *Wunsch and Heimbach*, 2007; *Macdonald et al*., 2009]. To estimate WBC transport at 30°S in the western South Pacific Ocean, *Mata et al*. [2000] combined WOCE repeat hydrographic surveys with moored recording current meter and acoustic Doppler current profiler measurements between 1991 and 1993. They described the East Australian Current (EAC) as a southward-oriented current positioned over the 2000 m isobath with a time-varying offshore limit of 40–100 km from the coast, flowing over a northward going countercurrent extending to 4000 m depth. According to *Mata et al*. [2000], the occasional meandering of the EAC offshore of the moored array leads to an underestimation of the average EAC transport and emphasizes the need for basin-spanning data sets and studies.

Wijffels et al. [2001] extended the work of *Mata et al*. [2000] across the Pacific using an inverse model forced with basin-crossing WOCE hydrographic data along the P6 section at 30°S–32°S and constrained with net flux of dissolved silica, a moored current meter array northeast of New Zealand, and a prescribed net northward flow feeding the Indonesian and Bering Strait throughflows. ALACE float measurements at 900 m depth were used to constrain the spatial distribution of the large-scale circulation field. Above the thermocline, their results show a basin-wide shallow counterclockwise subtropical gyre of thermocline and intermediate waters, and a broad southward flow off the coast of Chile, which corresponds to the Peru-Chile Undercurrent. Below the thermocline, they described a nearly closed recirculation in the deep region east of the Tonga Kermadec Ridge of northward bottom water, which returns southward as Pacific deep water, and a southward transport of Pacific deep water in the eastern boundary along the East Pacific Rise (EPR) and the Roggeveen Rise. A limitation in *Wijffels et al.*'s [2001] work is that snapshot sampling along P6 is inadequate to characterize the mean state of the flow field. The question of how the net basin-wide transport varies at interannual time scales was left to later data sets. Now a dozen years after the *Wijffels et al.*'s [2001] paper, there are 6 times as many Argo profiles and trajectories in 2012 as in the WOCE hydrographic and float data set in a 5° latitude band centered on 32°S. In this work, we take advantage of this increased number of float observations to develop improved estimates of the upper ocean volume transport, 0–2000 m, with a reference velocity based on Argo trajectories. This will allow us, without constraining the total transport, to improve on the previous estimates of the mean basin-wide transport at 32°S, its decomposition into the western and eastern boundary currents and interior flows, and its time variability during the Argo era.

The Southern Annular Mode (SAM) is the dominant mode of atmospheric low-frequency variability south of the extratropical regions of the Southern Hemisphere [*Thompson and Wallace*, 2000]. It is characterized by annular anomalies of opposite geopotential height in the Antarctic region and at southern midlatitudes. WOCE hydrographic measurements and Argo float profiles were used by *Roemmich et al*. [2007] to study the ocean circulation change in response to the strengthening of circumpolar westerly winds and the weakening of the midlatitude westerlies during the SAM increase of the 1990s. They found that changes in midlatitude wind stress curl are linked to an intensification of the South Pacific Ocean subtropical gyre. Using an Island Rule model forced with National Center for Environmental Prediction/National Center for Atmospheric Research wind stress and wind stress curl products, *Cai* [2006] described a strengthening of the southward EAC and of the northward interior transports tied to the intensification of the wind stress curl between the late 1970s and the early 2000s. According to coastal near-surface temperature and salinity time series measurements recorded on the path of the EAC extension, the trend of EAC flow strengthening related to the wind forcing can be traced back to the 1940s [*Hill et al*., 2008].

El Niño Southern Oscillation (ENSO) describes the low-frequency oscillation of sea surface temperature anomaly in the central and eastern equatorial Pacific. Observations [*Zilberman et al*., 2013] and numerical simulations [*Lee and Fukumori*, 2003] have investigated the time variability of the volume transport of the shallow Meridional Overturning Circulation in the tropical South Pacific Ocean. These studies have documented an ENSO signature in the volume transport at interannual time scales, characterized by a strengthening of the geostrophic transport in the interior and a weakening of the transport in the western Pacific during La Niña events. The reverse occurs during El Niño. The counteracting tendency of the transport was explained as a combined effect of two anticorrelated forcings: the off-equatorial wind stress curl in the western Pacific and the near-equatorial zonal wind stress in the interior Pacific.

Beyond addressing the time mean transport at 32°S, our goal in this paper is to answer the following questions: Is there any interannual variability in the basin-wide upper ocean transport at midlatitudes? What is causing it? Is the midlatitude transport affected by the SAM at interannual time scales? Do transport anomalies show an ENSO signature?

In this work, Argo profiles from 2004 to 2012 are used to estimate water mass pathways and velocities at 32°S in the upper 2000 m of the Pacific Ocean. This study exploits the increase in spatial and temporal coverage of the Argo data to improve on the earlier results obtained from WOCE data by *Wijffels et al*. [2001]. This paper is organized as follows: the data sets and methods are described in section 2. The mean circulation in the upper 2000 m at the western boundary and east of the dateline are presented in section 3. Interannual variability of the volume transport in relation to changes in the wind stress curl is considered in the same section. This analysis shows how interannual variations of the combined EAC and EAC recirculation transports are tied to the SAM. No evident ENSO-related signal was observed. The findings are summarized in section 4.

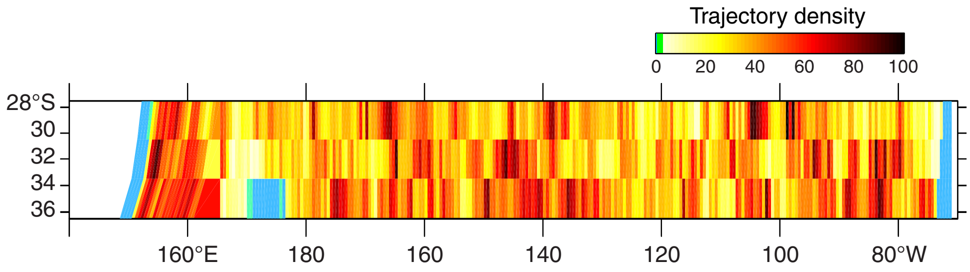

Figure 1. Float sampling density within 3° latitude × 1/2° longitude bins. Blue shows bins with no trajectories, and green shows bins with less than 3 float observations. In this projection, the latitude to longitude ratio is increased by a factor of 2.

2. Data and Methods

2.1. Argo Float Profiles and Trajectories

In this work, we use 1/6° × 1/6° gridded Argo data as described by *Zilberman et al*. [2013] for the January 2004 to December 2012 period, and unless otherwise specified all of our analysis is for the full 9 year period. The intrinsic resolution of the Argo data is coarser than 1/6°, but nevertheless features substantially smaller than 1° are robustly sampled in the mean field. Between 2004 and 2012, the number of Argo profiles obtained in each 1° × 1° box centered at 32°S is 36 in the mean field, and 4 in the time-varying field. The monthly mean and anomaly fields of temperature and salinity across the South Pacific Ocean (45°S–15°S, 140°E–70°W) are used to calculate geostrophic velocity, with the focus here on velocity across 32°S.

The MOC across the midlatitude South Pacific is characterized by bottom-to-deep volume transports of magnitude comparable to the thermocline and surface layers [*Wijffels et al*., 2001]. The choice of a reference level for geostrophic velocity calculations can be problematic. Transport estimates are computed with reference velocity at 1000 m based on Argo trajectories. Transports computed with reference velocity at 2000 m are shown for comparison. Argo trajectory data are used from the latitude range between 28°S and 34°S and for longitudes spanning the Pacific Ocean, for the time period 2004–2012. Observed float positions at the surface are extrapolated to surfacing and diving times following *Park et al*. [2005].

Different techniques were considered for binning the trajectory-based data. As will be shown in section 3, the circulation of the WBC region consists of the EAC flowing southward along the Australian coast and the EAC recirculation flowing northward offshore of the EAC. The coastline is oriented northwestward north of Brisbane and southwestward to the south of 32°S. We found that if we used north-south oriented bins in the WBC region, velocities of opposite signs were blended, and this attenuated the strength of the EAC. Instead, to preserve the sharp velocity gradients associated with the along-coast flow and flow reversal, trajectory-based velocities are sorted west of 164°E into 1/6° latitude × 1/2° longitude bins aligned with the 1000 m isobath. That is, the western most bins include all trajectories in the first 1/2° of longitude east of the 1000 m isobath and so on. The 1/6° latitude bins that parallel the 1000 m isobath are then grouped into 3° latitude bins. East of 164°E, trajectory-based velocities are sorted into 1/6° latitude × 1/2° longitude bins oriented north-south. To maximize the number of velocity observations per bin, trajectory data are regrouped and averaged into 3° latitude × 1/2° longitude grid cells (Figure 1). Float sampling density is heterogeneous near the coast of Chile (section 3.2.1). Bins were selected for further analysis if they contained at least 3 float observations within the 3° latitude × 1/2° longitude domain. Uncertainties are assigned based on the standard error, the standard deviation divided by the square root of the number of observations.

2.2. Climatological Products

The mean and the time variability of the wind stress curl, Ekman transport, and air-sea fluxes in the South Pacific are examined using reanalysis fields from the National Centers for Environmental Prediction (NCEP) and the European Centre for Medium-Range Weather Forecasts (ECMWF) Re-Analysis (ERA).

The NCEP fields are taken from the NCEP/National Center for Atmospheric Research (NCAR) archive. Data are available from the NCEP Web site (http://www.esrl.noaa.gov) [*Kalnay et al*., 1996]. The NCEP model version considered in this work uses a T62 Gaussian grid, which corresponds to a horizontal resolution of approximately 200 km. The momentum flux, surface sensible heat flux, surface latent heat flux, net longwave radiation, and net shortwave radiation are taken from the NCEP/NCAR monthly means of six hourly data.

The ECMWF fields are taken from the ERA/Interim archive available on the ECMWF Web site (http://data-portal.ecmwf.int/) [*Berrisford et al*., 2009]. The ERA/Interim reanalysis has a spectral T255 horizontal resolution, which corresponds to an effective grid resolution of approximately 100 km. The instantaneous surface stress is taken from the ECMWF monthly means of daily mean fields. The surface sensible heat flux, surface latent heat flux, surface solar radiation (shortwave radiation), and surface thermal radiation (longwave radiation) are taken from the ECMWF synoptic monthly mean archives.

2.3. Altimetry

Gridded altimetric sea surface height complementary to Argo is provided by Archiving, Validation, and Interpretation of Satellite Oceanographic data (AVISO) for studying the time variability of the geostrophic transport across the South Pacific. The AVISO fields used here are delayed time weekly fields of altimetric height anomaly projected onto a $1/3^\circ \times 1/3^\circ$ grid. In the AVISO archives, the sea surface height anomaly is computed relative to an 8 year mean from 1993 to 1999. In this study, the altimetry fields were adjusted to a 2004–2012 mean for consistency with the geostrophic transport anomalies derived using the Argo temperature and salinity profiles.

3. Results

Streamlines of relative geostrophic velocity on neutral density surfaces are computed using *Jackett and McDougall*'s [1997] method to provide a general picture of the flow field in the South Pacific Ocean as observed from the Argo data set (Figure 2a). Acceleration potential contours relative to 2000 dbar, as in *McDougall and Klocker* [2010, equation 62], averaged over the 2004–2012 time period on the neutral density surfaces 25.4 and 26.8 kg m^{-3} are shown in Figures 2b and 2c. The 25.4 kg m^{-3} neutral density surface is chosen to lie in the midlatitude pycnocline, within the core of the EAC and the surface-intensified flow field in the interior [*Wijffels et al*., 2001]. The 26.8 kg m^{-3} neutral density surface is chosen for its proximity to the lower bound of the EAC [*Mata et al*., 2000; *Wijffels et al*., 2001] and further east to the lower bound of Subtropical Mode Waters [*Sato and Suga*, 2009]. For clarity, the South Pacific Ocean is divided into three regions: the western Pacific (west of the dateline), the interior (180°W–95.4°W), and the eastern Pacific (east of 95.4°W) (Figure 2a).

In the eastern Pacific, the streamlines running equatorward off the South American coast are indicative of the Peru-Chile Coastal Current (PCC) (Figures 2b and 2c). The PCC turns west at about 10°S–20°S and merges with the South Equatorial Current. Onshore of the PCC, the Peru Chile Undercurrent (PCUC), mainly fed by Equatorial Undercurrent and Southern Subsurface Countercurrent waters [*Montes et al*., 2010], flows poleward along the shelf break. A broad equatorward flow is seen in the streamlines in the subtropical gyre interior. At the western boundary, the streamlines running poleward along the Australian coast are the signature of the EAC. The EAC splits at around 30°S–32°S, with shallow layers mainly turning eastward into the Tasman Front (TF) and deep flow continuing along the coast as the EAC extension (EACex), in agreement with historical hydrographic observations by *Tilburg et al*. [2001]. The TF meanders across the Tasman Sea to the northern coast of New Zealand (NZ), where it becomes the East Auckland Current (EAuC).

3.1. Mean Geostrophic Velocity in the EAC

The 2004–2012 mean meridional geostrophic velocity in the western boundary region is shown in Figure 3a for 30°S and in Figure 3b for 32°S with the reference velocity at 1000 m from Argo trajectories. For the Australian continental shelf region and on the crest of the Norfolk Ridge, where depth is shallower than 1000 m, the velocity is computed relative to the bottom. In regions deeper than 1000 m where there are fewer than three trajectories within 3° latitude × 1/2° longitude, the velocity at 1000 m depth is set relative to 2000 m (Figure 1). This includes the Norfolk Ridge region and the eastern boundary (Figure 2a). West of 155°E, the meridional geostrophic velocity is southward ($v_g < 0$) both at 30°S and 32°S, consistent with the shoaling of the pycnocline from east to west. The highest mean velocities west of 154.5°E ($v_g < -0.2$ m s^{-1}) are signatures of the EAC. The amplitude of the meridional geostrophic velocity within the EAC is in good agreement with observations by *Mata et al*. [2000]. The core of the EAC, observed adjacent to the coast at

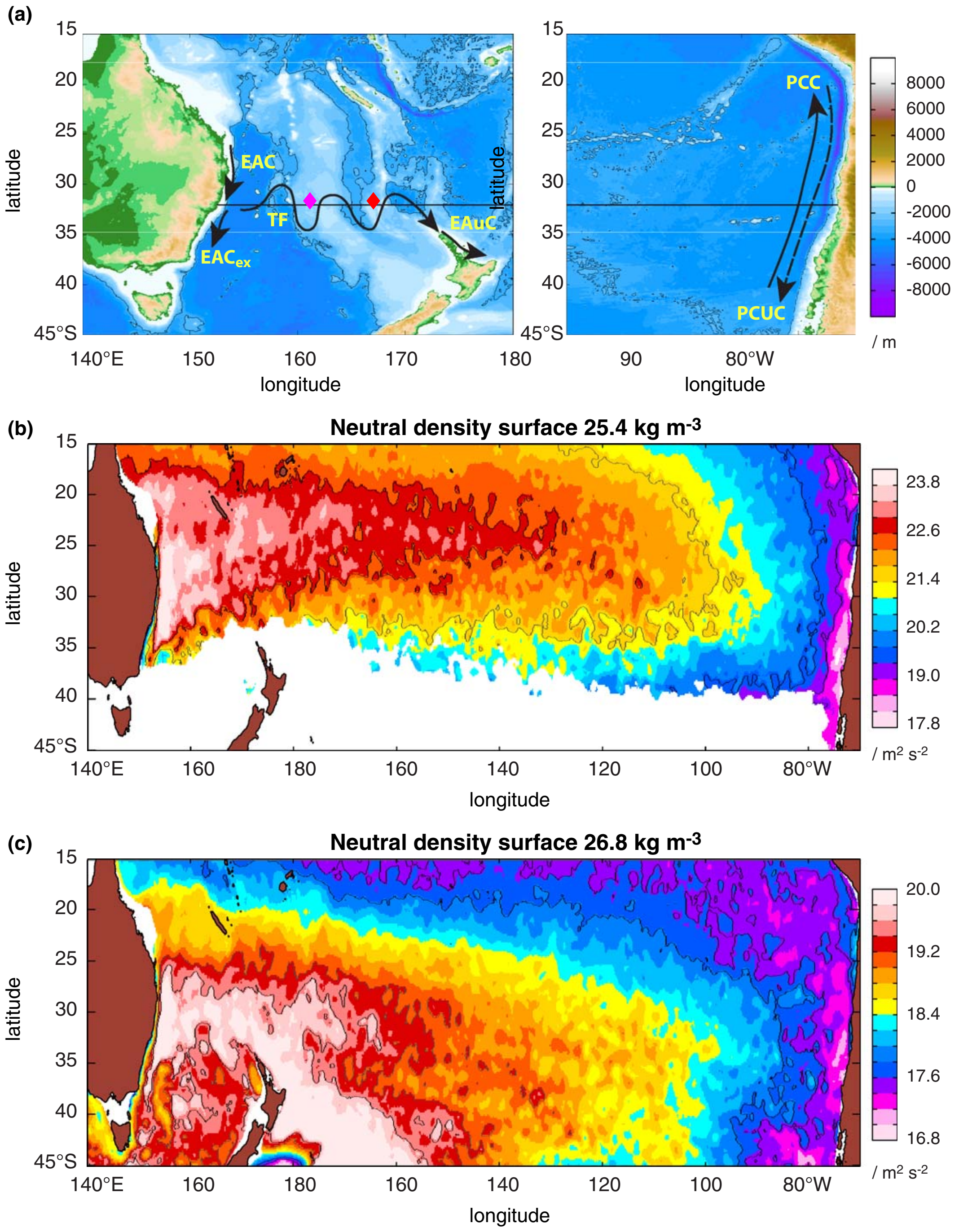

Figure 2. (a) Schematic of the general circulation in the subtropical South Pacific Ocean at midlatitudes (black arrows) in the western and eastern regions. The underlying color gives the ETOPO2 2 min bathymetry with the black contour indicating the 3000 m isobath. The pink diamond indicates the Lord Howe Rise. The red diamond indicates the Norfolk Ridge. The continuous black line indicates 32°S. The dashed lines in black indicate 180° and 95.4°W. (b) Acceleration potential contours relative to 2000 dbar 19.1, 19.7, 21.5, and 22.6 $m^2 s^{-2}$ averaged from 2004 to 2012 on the neutral density surface 25.4 kg m^{-3}. (c) Acceleration potential contours 17.57, 17.8, 19.2, and 19.55 $m^2 s^{-2}$ averaged from 2004 to 2012 on the neutral density surface 26.8 kg m^{-3}.

30°S, moves offshore at 32°S as the coastline curves to the west. The elevated northward velocities ($v_g > 0.05$ m s^{-1}) east of 155°E are indicative of the EAC recirculation, where the current interacts with the Lord Howe Rise [*Mata et al.*, 2000]. The strength of the EAC recirculation increases from 30°S to 32°S, in agreement with observations by *Ridgway and Dunn* [2003]. At 32°S, northward flow below the EAC is indicative of the EAC Countercurrent [*Mata et al.*, 2000]. Southward flow below the EAC recirculation is the

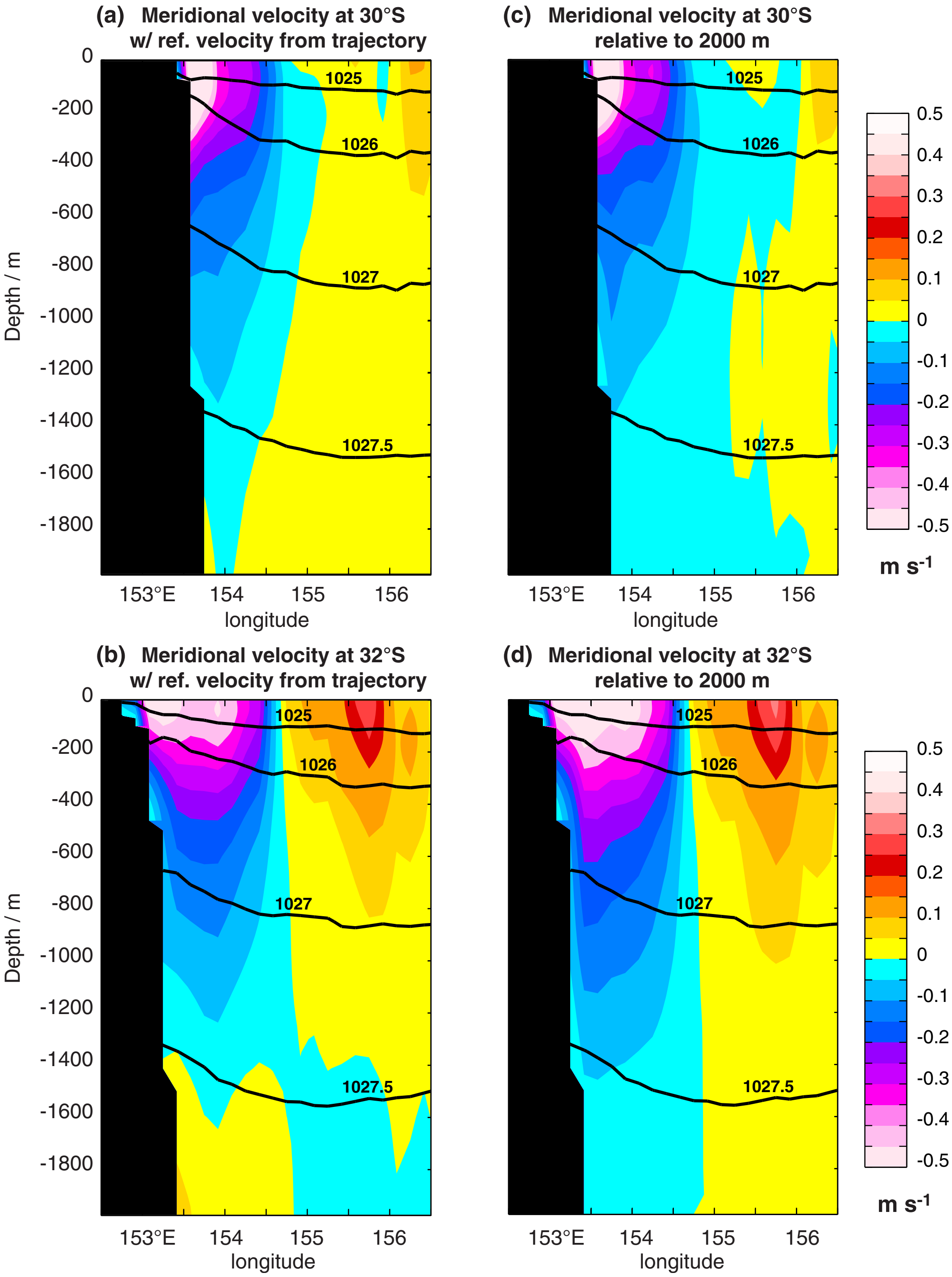

Figure 3. (a and c)Meridional geostrophic velocity in the EAC at 30°S and (b and d) 32°S averaged from 2004 to 2012 with reference velocity using trajectories (Figures 3a and 3b) and relative to 2000 m depth (Figures 3c and 3d). The black lines correspond to 2004–2012 mean potential density contours (kg m^{-3}).

signature of the EAC extension [*Tilburg et al.*, 2001]. Figure 4 compares integrated transport using the trajectories to determine a reference (thick red line) against transport using a 2000 m level of no motion. When a level of no motion at 2000 m depth is used, the meridional geostrophic velocity at 1000 m is more negative below the core of the EAC and more positive in the lower part of the EAC recirculation. As a result, the core of the EAC and the EAC recirculation deepen, and the signatures of the EAC Countercurrent and EAC

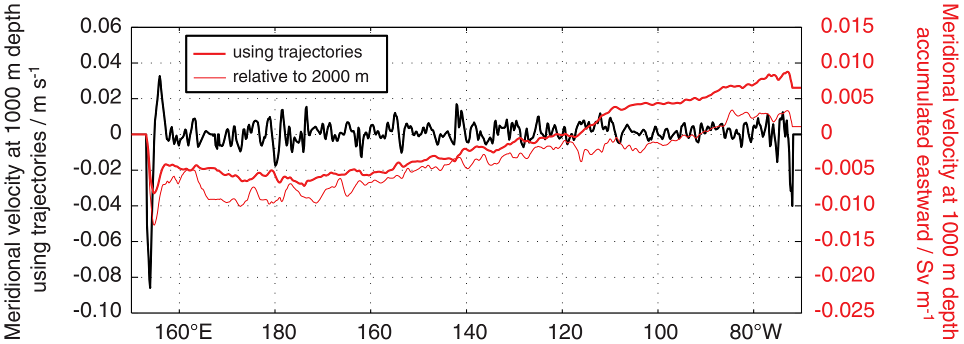

Figure 4. The black line indicates the meridional velocity at 1000 m depth using 2004–2012 Argo float trajectories with 3° latitude × 1/2° longitude bins centered at 32°S. The red lines indicate the meridional velocity at 1000 m depth accumulated eastward based on 2004–2012 Argo float trajectories with 3° latitude × 1/2° longitude bins centered at 32°S (thick red line) and using a level of no motion at 2000 m depth (thin red line).

extension, seen when using trajectory-based reference velocities, disappear in the velocity computations based on a 2000 m level of no motion (Figures 3a–3d).

3.2. Mean Transport at 32°S

3.2.1. Volume Transport

Best estimates of the mean meridional transport are computed using the meridional geostrophic transport with reference velocity at 1000 m based on Argo trajectories and systematic errors in the vertical shear. Error bars depend on trajectory density per 3° latitude × 1/2° longitude bin.

At 32°S, the 2004–2012 mean basin-wide meridional geostrophic transport in the upper 2000 m is 22.3 Sv equatorward, here computed with gridded Argo temperature and salinity profiles and reference velocity based on Argo trajectories (V_g). If instead we use a level of no motion at 2000 m depth, the basin-wide meridional geostrophic transport is 10.9 Sv, 11.4 Sv lower than computed using float trajectories (Figure 5). The discrepancy between the transport estimates arises from more negative velocities in the EAC region at 1000 m when a reference level of no motion at 2000 m depth is used rather than float trajectories, and a sharp increase in the trajectory-based velocities at 1000 m between 117°W and 107°W (Figure 4). Between 30.5°S and 33.5°S, the northward flow of intermediate and deep waters east of the dateline is faster adjacent to the EPR (Figure 6). According to observations by N. V. Zilberman et al. (Deep flow acceleration over the Eastern Pacific Rise, in preparation, Estimating meridional transport in the East Australian Current, in preparation), the flow acceleration over the EPR extends from 40°S to 20°S.

Uncertainties in trajectory-based geostrophic transport at 32°S arise from heterogeneous trajectory density. Random errors (based on variability) in trajectory-based velocity at 1000 m computed for each 3° latitude × 1/2° longitude bin represent about 25% of the bin-averaged velocity (Figures 3b, 3d, and 7a). The largest errors are seen at the western boundary, where the standard deviation is highest, and at the eastern boundary, where the trajectory density per bin is lowest (Figures 7b and 7c). Assuming the estimates from 1/2° longitude bins are independent, the uncertainty in transport is 4.2 Sv in the western Pacific, 4.1 Sv in the interior, 2.2 Sv in the eastern Pacific, and 6.0 Sv basin wide. In the western boundary region, random errors are 2.9 Sv for the EAC and 3.6 Sv for the EAC recirculation.

Systematic errors are generated by the mean vertical shear during the float ascent and descent between surface and parking depth. Assuming that the rising and descending times of a float represent 5% of its cycle, systematic errors are −0.8 Sv in the western Pacific, 1.6 Sv in the interior, 0.9 Sv in the eastern Pacific, and 1.7 Sv basin wide. In the western boundary region, systematic errors are −2.5 Sv for the EAC and 1.7 Sv for the EAC recirculation. The time-varying shear contributes to the random error described above.

Based on random and systematic errors, our best estimate of the 2004–2012 mean basin-wide meridional geostrophic transport in the upper 2000 m is 20.6 ± 6.0 Sv equatorward. Our best estimate of the EAC transport [$(V_g)_{EAC}$], defined as the maximum southward transport integrated eastward across 32°S, is 23.3 ± 2.9 Sv (Figure 5). The offshore limit of the 2004–2012 mean EAC is 154.5°E. Our estimate of $(V_g)_{EAC}$ is 1.2 Sv higher than moored observations by *Mata et al.* [2000] and 6.7 Sv lower than constrained transport

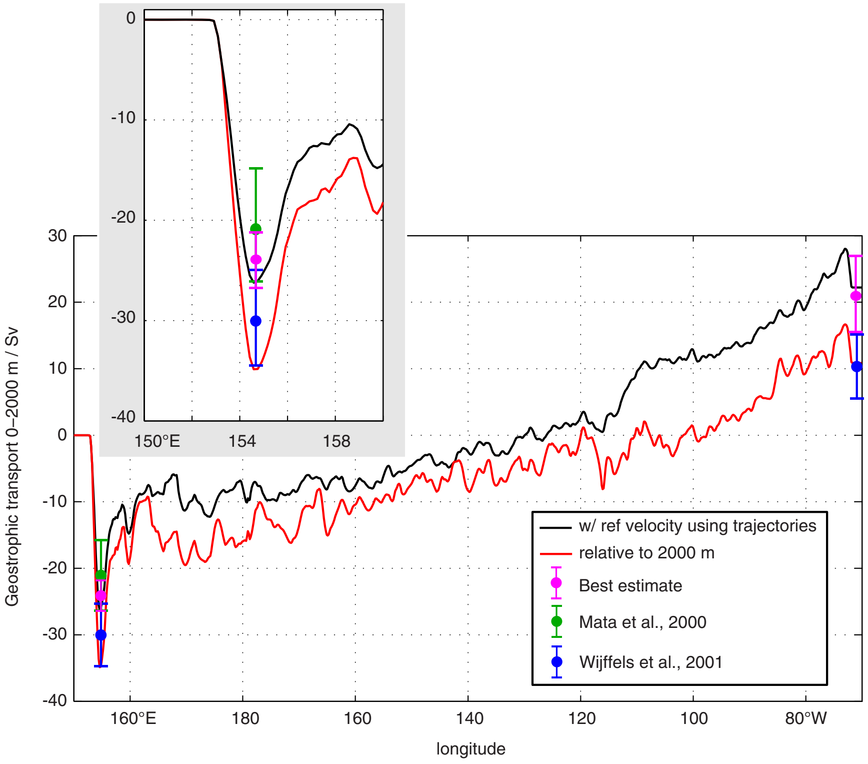

Figure 5. Geostrophic transport accumulated eastward from the eastern coast of Australia at 32°S with reference velocity from trajectories (black) and relative to 2000 m (red) averaged from 2004 to 2012. Also indicated are transport estimates by *Mata et al*. [2000] (green) and *Wijffels et al*. [2001] (blue). The error bars indicate the uncertainties in the transport estimates.

estimates by *Wijffels et al*. [2001] collected at 30°S. *Mata et al*. [2000] may have underestimated the EAC transport since the offshore limit of the EAC extends beyond their mooring line. The recirculation of the geostrophic transport between the offshore limit of the EAC and the dateline [$(V_g)_{recirc}$] of 16.3 $\pm$ 3.6 Sv is partly a signature of the meandering of the TF (Figure 5). The 2004–2012 mean meridional geostrophic transport at 32°S is 7.0 $\pm$ 4.2 Sv southward in the western Pacific [$(V_g)_{west} = (V_g)_{EAC} + (V_g)_{recirc}$], 18.4 $\pm$ 4.1 Sv northward in the interior [$(V_g)_{interior}$], and 9.2 $\pm$ 2.2 Sv northward in the eastern Pacific [$(V_g)_{east}$]. The northward transport offshore of the coast of Chile is indicative of the PCC. The elevated northward velocities ($v_g > 0.08$ m s^{-1}) in the upper 200 m (not shown) are in good agreement with observations by *Reid* [1973]. East of the PCC, the southward flow is a signature of the PCUC. The highest southward velocities ($v_g < -0.1$ m s^{-1}) at 200 m depth indicate the core of the PCUC (not shown) and are in agreement with current meter measurements by *Shaffer et al*. [1999].

In the upper 1100 m, the trajectory-based basin-wide transport is northward and consists of a strong component above 200 m and a decrease from 200 m to 1100 m (Figure 8). If we use a level of no motion at 2000 m, the geostrophic transport is northward, with similar shape to the trajectory-based estimate, but of smaller magnitude. Below 1100 m depth, the transport relative to 2000 m is southward, implying poleward

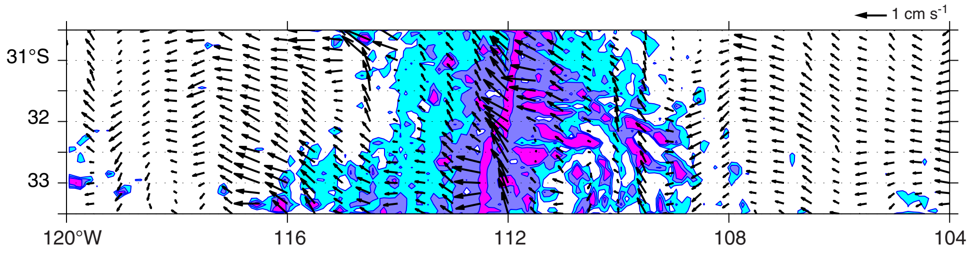

Figure 6. The black arrows indicate velocity vectors computed using Argo float trajectories at 1000 m depth. The underlying color shows bathymetry contours. Pink indicates bottom depth of 2600 m, purple is for 2800 m, and blue is for 3000 m.

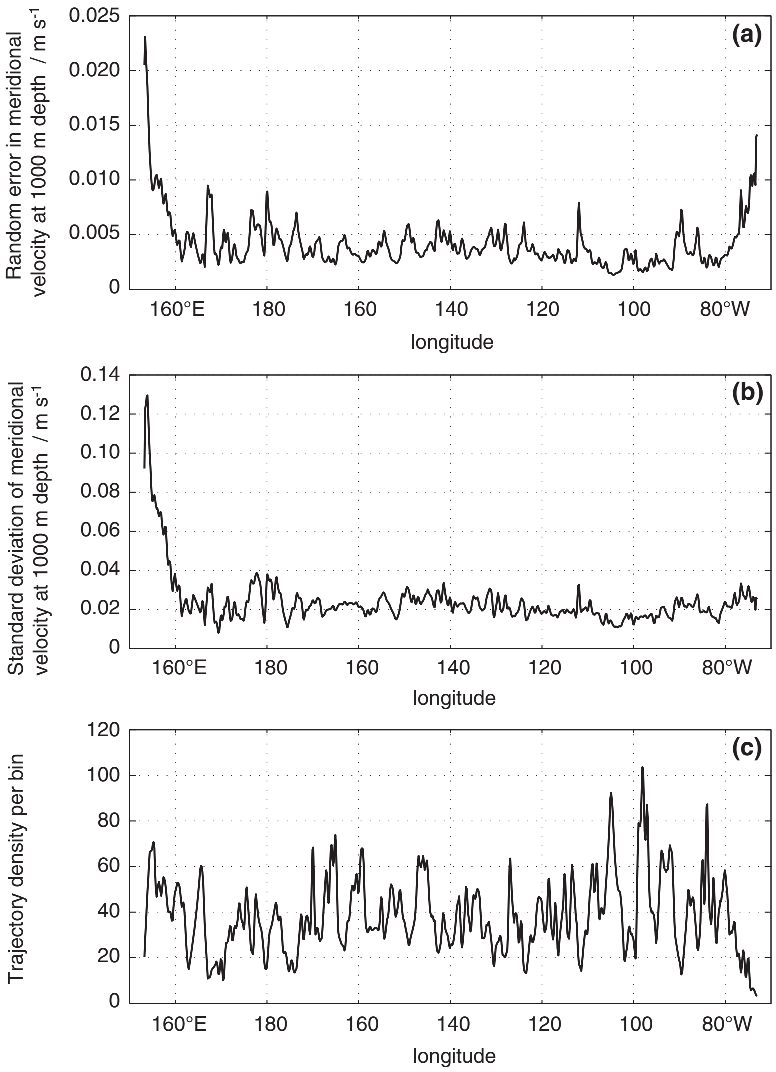

Figure 7. (a) Random error in meridional velocity at 1000 m depth, (b) standard error of meridional velocity at 1000 m depth, and (c) trajectory density per bin using 2004–2012 Argo float trajectories with 3° latitude × 1/2° longitude bins centered at 32°S.

return of the deep Meridional Overturning Circulation, in agreement with constrained transport estimates by *Wijffels et al.* [2001]. In contrast, the trajectory-based transport is northward and is characterized by a slight increase within the same depth range. This suggests that the poleward return of deep water flow occurs below 2000 m depth. The differences in shear between our estimates and *Wijffels et al.*'s [2001] suggest that a single P6 hydrographic transect is not representative of the mean in the 0–1500 m depth range. Argo-based geostrophic transport estimates are better determined in the upper 1500 m of the water column relative to the 1500–2000 m depth range. Limitations lie primarily in the uncertainty introduced by the reduced number of float profiles used in the gridded data products below 1500 m depth. An analysis of the mean geostrophic transport below 2000 m depth is beyond the scope of this work.

The Indonesian throughflow (ITF) is the only water mass pathway between the Pacific and Indian Oceans north of 32°S. In the subtropical South Pacific, the deep Meridional Overturning Circulation (MOC) closes below about 1000 m [*Wijffels et al.*, 2001], and the shear between 1000 and 2000 m is weak. Assuming conservation of mass within a box representing the 0–2000 m depth range of the Pacific Ocean north of 32°S, we compute the time-varying volume transport of the ITF

$$V_{ITF} = -(V_g + V_{Ek} - V_{BS} + W_{2000}) + (E - P), \tag{1}$$

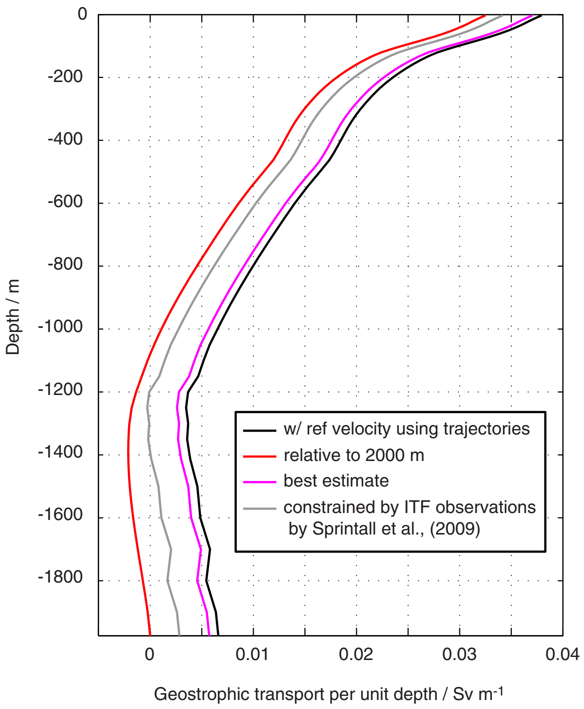

Figure 8. The 2004–2012 mean basin-wide geostrophic transport per unit depth computed at 32°S with reference velocity from trajectories (black), relative to 2000 m (red), best estimate with reference velocity from trajectories including systematic error (magenta), and constrained by ITF observations by *Sprintall et al.* [2009] (gray).

where V_{Ek} is the basin-wide Ekman transport at 32°S, V_{BS} is the Bering Strait transport set to 0.8 Sv as reported by *Coachman and Aagaard* [1998], $W_{2000}=\int_A w(z=2000)dA$ is the vertical transport at 2000 m over all of the Pacific north of 32°S, A is the surface area of the Pacific Ocean north of 32°S, $w(z)=(\partial\rho/\partial t)/(\partial\bar{\rho}/\partial z)$ is the time-varying vertical velocity, ρ is the potential density, E is the evaporation, and P is the precipitation over all of the Pacific north of 32°S. At 32°S, the 2004–2012 mean V_{Ek} computed using ECMWF reanalysis is 0.6 Sv and -0.2 Sv using NCEP. If the change in density at 2000 m over the Pacific north of 32°S, 2004–2012, is indicative of net vertical velocity, then the net vertical transport is -0.9 Sv. Vertical diffusion is not considered in the computation of the vertical velocity. The magnitude of evaporation minus precipitation is 0.04 Sv using ECWMF and -0.3 Sv using NCEP north of 32°S. The 2004–2012 mean V_{Ek} and $(E-P)$ are small compared to our best estimate of the 2004–2012 mean V_g.

The 2004–2012 mean V_{ITF} computed using our best estimate of V_g is 21.0 Sv using ECMWF for V_{Ek} and $(E-P)$, and 20.6 Sv using NCEP. The midvalue between V_{ITF} estimates using NCEP and ECMWF is 20.8 Sv, higher than the 2004–2006 mean of 15 Sv by *Sprintall et al.* [2009]. The error uncertainty of 6.0 Sv in V_g associated with the error in trajectory-based velocity at 1000 m gives a V_{ITF} range of 14.8–26.8 Sv, consistent with ITF range of 10.7–18.7 Sv by *Sprintall et al.* [2009] from 2004 to 2006. Applying a uniform poleward velocity of 0.02 cm s^{-1} to our best estimate of V_g leads to a V_{ITF} of 15 Sv, equal to *Sprintall et al.* [2009]. In the upper 2000 m, the constrained transport is oriented northward and lies between our best estimate of V_g and the transport relative to 2000 m (Figure 8).

3.2.2. Heat Budget in the Pacific Ocean North of 32°S

The heat budget north of 32°S is given by

$$S=H+Adv_z+Q. \qquad (2)$$

As noted in section 3.2.1, the 2004–2012 mean Ekman transport at 32°S is negligible compared to the geostrophic transport. The heat transport is estimated as the heat flux convergence into the region north of 32°S, based on the best estimate of the basin-wide geostrophic transport (20.6 Sv) and temperature difference between waters entering and leaving the region.

The heat transport is

$$H=-\rho_0 c_p (T_g-T_{ITF})V_g, \qquad (3)$$

where T_g is the temperature of V_g, and T_{ITF} is the temperature of V_{ITF}. The 2004–2012 mean T_g is 12.6°C. T_{ITF} is set to 17.9°C as reported by *Sprintall et al.* [2009].

The vertical advection of heat north of 32°S is

$$Adv_z=\rho_0 c_p (T_{2000}-T_{ITF})W_{2000}, \qquad (4)$$

where T_{2000} is the temperature of W_{2000}. The 2004–2012 mean T_{2000} is 2.2°C.

Table 1. Heat Transport Into the Region North of 32°S (H), Vertical Advection of Heat (Adv_z), Heat Storage in the Upper 2000 m (S), Air-Sea Flux (Q), and Residual of the Oceanic Heat Transport, Vertical Advection of Heat, Heat Storage, and Air-Sea Flux ($H + Adv_z - S + Q$) in the Region North of 32°S Averaged From 2004 to 2012 Using NCEP and ECMWF

	NCEP	ECMWF
H/PW	-0.43 ± 0.13	
Adv_z/PW	$+0.06$	
S/PW	-0.02	
Q/PW	$+0.75$	$+1.04$
$H + Adv_z - S + Q$/PW	$+0.40$	$+0.69$

The heat storage north of 32°S is

$$S = \int_A \int_{2000}^{0} \rho_0 c_p \frac{\partial T}{\partial t} dz dA, \tag{5}$$

where A is the surface area of the Pacific Ocean north of 32°S and T is the temperature. The vertical diffusion rate at 2000 m depth north of 32°S, computed using a vertical diffusivity coefficient of 10^{-4} m^2 s^{-1} [*Munk and Wunsch*, 1998], is small compared to H, Adv_z, and S in equations (3)–(5). The contribution of the vertical diffusion to the heat budget is not included in our analysis.

The air-sea heat flux north of 32°S is

$$Q = \int_A Q_l + Q_s + Q_{lw} + Q_{sw} dA, \tag{6}$$

where Q_l is the latent heat of evaporation, Q_s is the sensible heat flux induced by the temperature difference between the ocean and the atmosphere, Q_{lw} is the net longwave radiative flux, and Q_{sw} is the net shortwave radiative flux.

The 2004–2012 mean heat transport at 32°S, H in equation (3), and the air-sea flux north of 32°S, Q in equation (6), are significantly larger than the vertical advection of heat and heat storage north of 32°S, Adv_z and S, in equations (4) and (5) and Table 1.

The region north of 32°S gains heat from the atmosphere ($Q > 0$) and loses heat in the upper 2000 m ($H < 0$). The 2004–2012 mean heat transport is -0.43 ± 0.13 PW, consistent with the heat transport estimate by *Talley* [2003] at 28°S, and smaller than implied by air-sea heat flux north of 32°S (Table 1). The error uncertainty of 0.13 PW in H is associated with error in trajectory-based velocity at 1000 m.

The residual of the oceanic heat transport, heat storage, vertical advection of heat, and air-sea flux in the region north of 32°S is 0.69 PW using ECMWF and 0.40 PW using NCEP (Table 1). This residual is 4.3 W m^{-2} for ECMWF and 2.5 W m^{-2} for NCEP, smaller than systematic errors in the reanalysis air-sea fluxes as reported by *Grist and Josey* [2003].

3.2.3. Water Mass Transport

The water mass transport at 32°S is partitioned into the western Pacific, the interior, and the eastern Pacific (Figure 9). For each region, the trajectory-based transports are binned in T-S space (Figures 10–12), with bins 1°C by 0.1 psu wide. Also represented are trajectory-based transports per °C summed across all salinities, and per 0.1 psu of salinity, summed across all temperatures. The T-S and planetary potential vorticity characteristics of the water masses are described in Table 2.

At the eastern boundary, the water mass transport in the upper thermocline consists of fresh and warm surface waters and South Pacific Eastern Subtropical Mode Waters (SPESTMW) carried northward in the PCC (Figures 9a and 10a–10c). The planetary potential vorticity minimum of 2–3 × 10^{10} m^{-1} s^{-1} seen in Figure 9b between 25 and 25.7 kg m^{-3} is indicative of SPESTMW, formed as deep late-winter mixed layers in the eastern South Pacific north of the Subtropical Front [*Tsuchiya*, 1998; *Wong and Johnson*, 2003; *Sato and Suga*, 2009]. In the mid and lower thermocline, we see a two-way transport of fresh and cool Eastern South

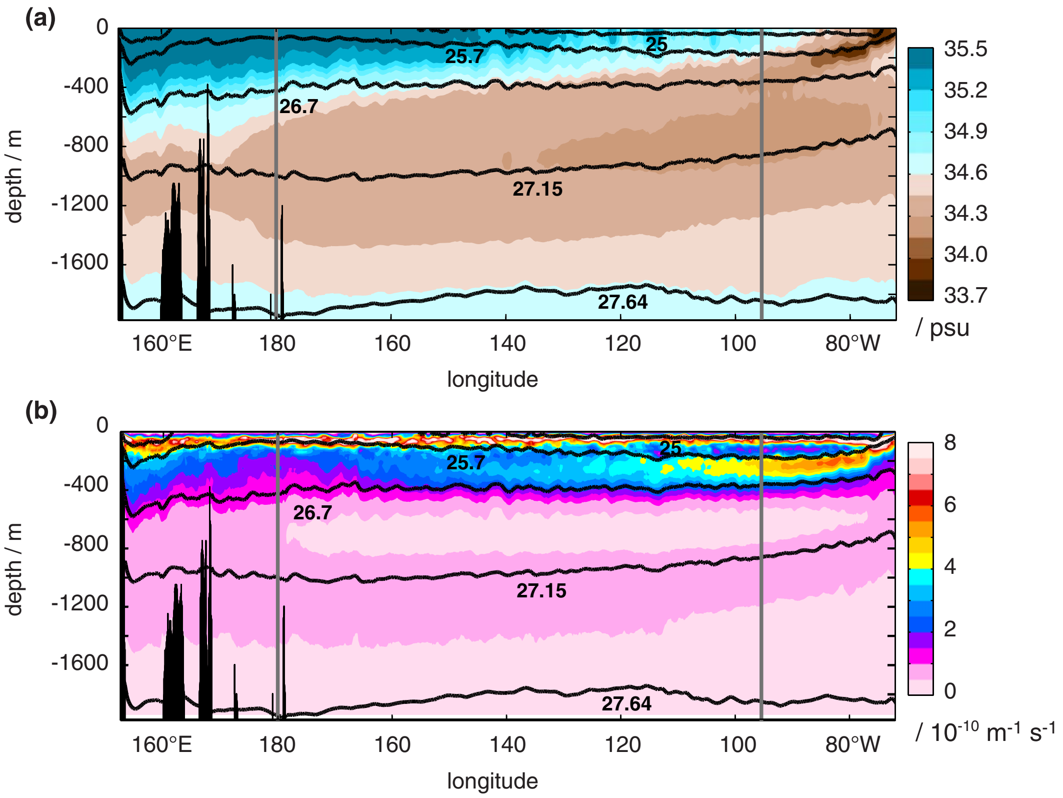

Figure 9. (a) Salinity and (b) absolute planetary potential vorticity averaged from 2004 to 2012 at 32°S. The black lines correspond to 2004–2012 mean potential density anomaly contours (kg m^{-3}). The gray lines indicate the boundaries between the western Pacific (west of the dateline), the interior (180°W–95.4°W), and the eastern Pacific (east of 95.4°W).

Pacific Intermediate Waters (ESPIW), Subantarctic Mode Waters (SAMW), and Antarctic Intermediate Waters (AAIW) flowing northward in the PCC, and southward in the PCUC (Figure 10). The shallow salinity minimum seen in Figure 10c below the SPESTMW is indicative of the ESPIW, which originates from the eastward freshening of western Pacific subsurface waters along the southern rim of the subtropical gyre [*Karstensen*, 2004]. The SAMW seen below is formed from sinking just north of the Subantarctic Front of eastern Pacific waters freshened by an excess of precipitation over evaporation [*Talley*, 2008]. The deep salinity minimum helps define the AAIW as the freshest variety of SAMW. Net northward volume transport primarily occurs within temperature ranges of SPESTMW and AAIW (Figure 10b). The transport maxima of 1–2 Sv are seen within the temperature and salinity bins of the SAMW and AAIW. In the midthermocline, the transports of ESPIW in the PCC and in the PCUC have similar amplitude and opposite sign, which implies a small net volume transport.

In the interior, T-S diagrams indicate saltier and warmer subsurface waters (Figures 11a–11c) compared with the eastern boundary (Figures 10a–10c). The fresher and cooler conditions in the east result from the weakening of the Subtropical Front and northward advection of SAMW in the PCC. Net transport in temperature and salinity bins is mostly northward. As is also true in the eastern boundary, the T-S bins with highest transport ($>$1 Sv) occur within the SAMW and AAIW. During the time that the eastern Pacific AAIW is carried anticlockwise around the subtropical gyre, the salinity at its core slowly increases through mixing with higher salinity water from above and below. The maxima in transport per 0.1 psu in the interior show AAIW to be saltier than in the eastern boundary (Figures 10c and 11c).

The T-S relation at the western boundary (Figure 12) appears much tighter than in the interior (Figure 11) or at the eastern boundary (Figure 10). The Southwestern Subtropical Mode Waters (SWSTMW) are saltier than the subsurface waters to the east, indicating that precipitation minus evaporation is greater along the Subtropical Front east of NZ than in the Tasman Sea. Beyond the EAC bifurcation, a broad T-S range of SWSTMW, SAMW, and AAIW flows southward in the EACex (Figures 12a–12c). In contrast, only the warmest

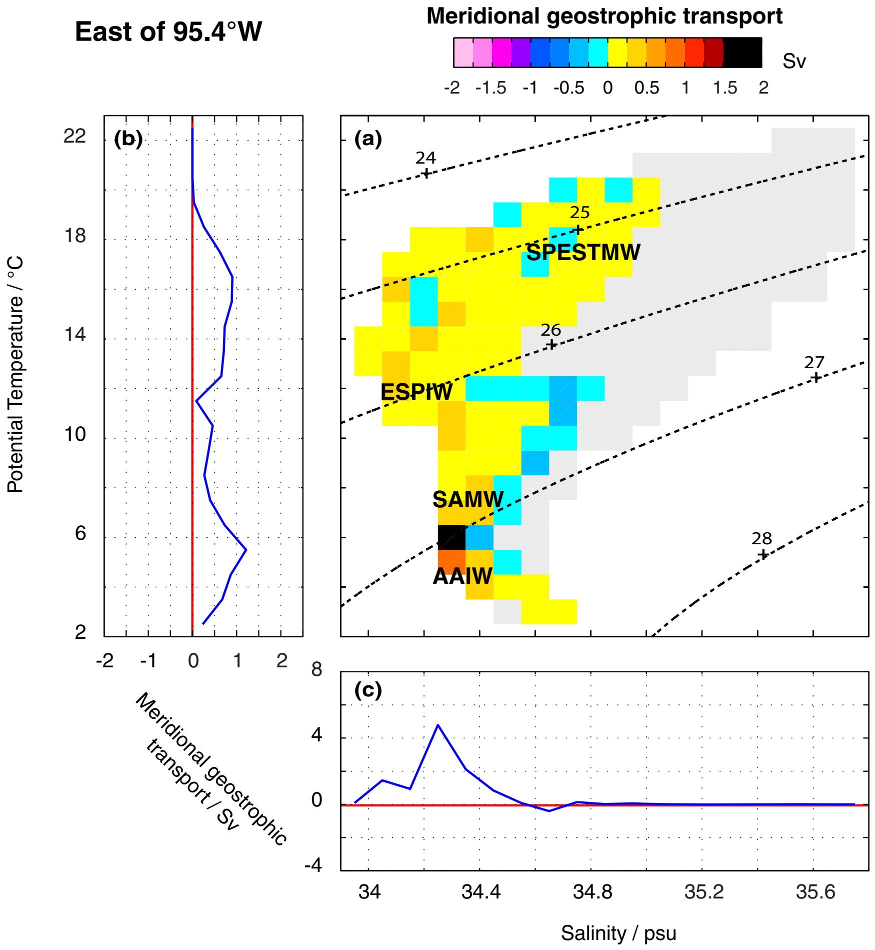

Figure 10. Trajectory-based transport east of 95.4° at 32°S (a) separated into 1.0°C by 0.1 psu bins, (b) per unit temperature (°C) summed across all salinities, and (c) per 0.1 psu of salinity summed across all temperatures, averaged from 2004 to 2012. Northward transport is positive. The black lines correspond to 2004–2012 mean potential density anomaly contours (kg m^{-3}). In gray is represented the basin-wide transport at 32°S separated into 1.0°C by 0.1 psu bins.

part of the SWSTMW core and a limited amount of denser waters recirculate northward in the TF. According to *Tomczak* [2006], the AAIW of the Tasman Sea may form by subduction along the Polar Front between Tasmania and NZ or off the eastern coast of South America. AAIW formed in the southwestern Pacific is

Table 2. Temperature, Salinity, and Absolute Planetary Potential Vorticity Characteristics of South Pacific Eastern Subtropical Mode Water (SPESTMW), Southwestern Subtropical Mode Water (SWSTMW), Intermediate Water (ESPIW), Subantarctic Mode Water (SAMW), and Antarctic Intermediate Water (AAIW) in the South Pacific Ocean

Mode Water	Temperature (°C)	Salinity (psu)	Density (kg m^{-3})	Absolute Planetary Potential Vorticity (10^{-10} m^{-1} s^{-1})
SPESTMW[a]	13–26.0		24.5–25.8	<2.5
SWSTMW[b]	15–19<2°C/100 m			
ESPIW[c,d]	11–13	34.1–34.3 shallow salinity minimum	25.75–26.25	
SAMW[e,f]	4.0–15.0	34.2–35.8	26.5–27.1	Absolute planetary potential vorticity minimum
AAIW[g]	2–10	33.8–34.5 deep salinity minimum	27–27.3	

[a] *Sato and Suga* [2009].
[b] *Cornuelle and Roemmich* [1992].
[c] *Schneider et al.* [2003].
[d] *Karstensen* [2004].
[e] *McCartney* [1977].
[f] *Hanawa and Talley* [2001].
[g] *Emery* [1983].

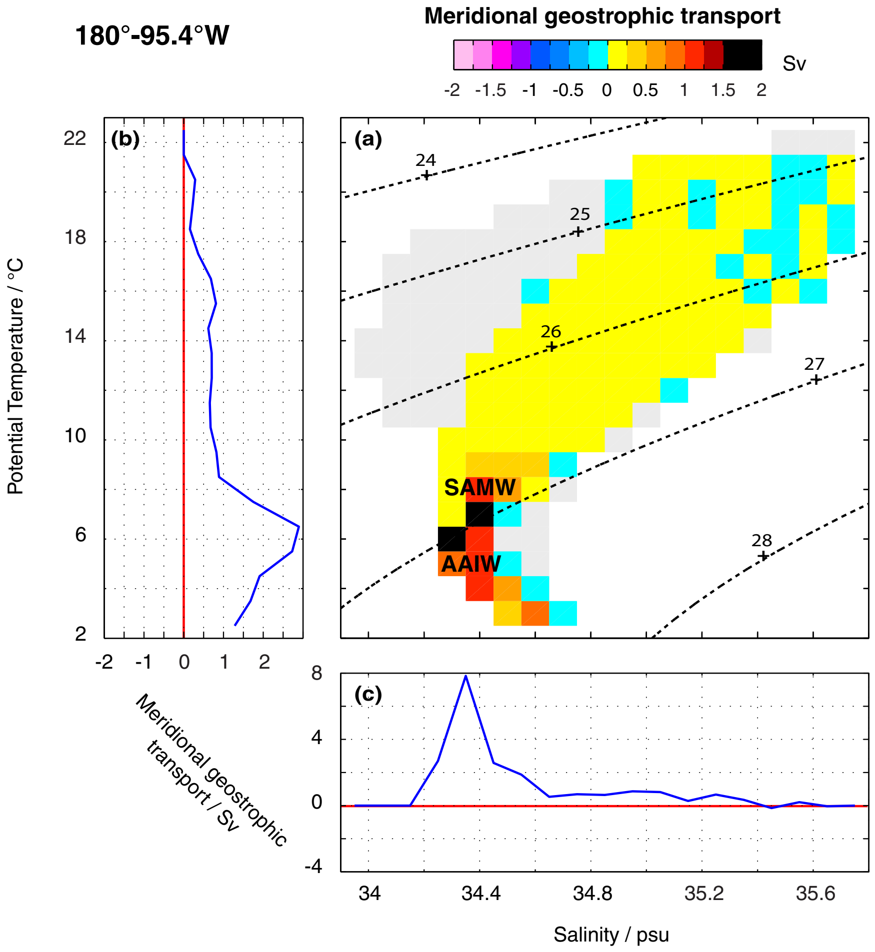

Figure 11. Trajectory-based transport between 180° and 95.4° at 32°S (a) separated into 1.0°C by 0.1 psu bins, (b) per unit temperature (°C) summed across all salinities, and (c) per 0.1 psu of salinity summed across all temperatures, averaged from 2004 to 2012. Northward transport is positive. The black lines correspond to 2004–2012 mean potential density anomaly contours (kg m^{-3}). In gray is represented the basin-wide transport at 32°S separated into 1.0°C by 0.1 psu bins.

characterized by a salinity lower than 34.3, while AAIW formed in the eastern Pacific is saltier. Our measurements reveal AAIW with salinities in the 34.5–34.6 range, indicative of AAIW of eastern Pacific origin (Figure 12c).

The basin-wide volume transport at 32°S consists of equatorward volume transport of 7.3 ± 0.9 Sv of surface and mode waters above 26.5$\sigma_\theta$kg m^{-3}, 4.9±1.0Sv of SAMW between 26.5σ_θ and 27σ_θ kg m^{-3}, and 4.9 ± 1.4 Sv of AAIW between 27σ_θ and 27.3σ_θ kg m^{-3} (Table 3). *Hartin et al*. [2011] use hydrographic and chlorofluorocarbon (CFC) data collected within the South Pacific in the austral winter of 2005 to calculate formation rates for the SAMW and AAIW. The CFC-derived formation rates of 7.3 ± 2.1 Sv for SAMW and 5.8 ± 1.7 Sv for AAIW that circulate within the South Pacific subtropical gyre are consistent with our equatorward volume transport estimates at 32°S.

3.3. Interannual Variability of the Transport at 32°S

Relative to the 2004–2012 mean, the geostrophic transport anomalies of the poleward EAC and equatorward EAC recirculation exhibit a SAM signature characterized by an increase during the positive phase of the SAM and a decrease during the negative phases of the SAM (Figure 13a). The correlation coefficient of [$(V_g)_{EAC}$] and [$(V_g)_{recirc}$] with the SAM index is 0.6 for the 1 year smoothed time series. The SAM index used in this work is based on the NOAA Optimal Interpolation 700 hPa height anomalies for the 30 year period 1979–2012, poleward of 20° latitude in the Southern Hemisphere (http://www.cpc.ncep.noaa.gov/products/precip/CWlink/daily_ao_index/aao/) [*Mo*, 2000]. By positive phases of the SAM, we refer to times when the

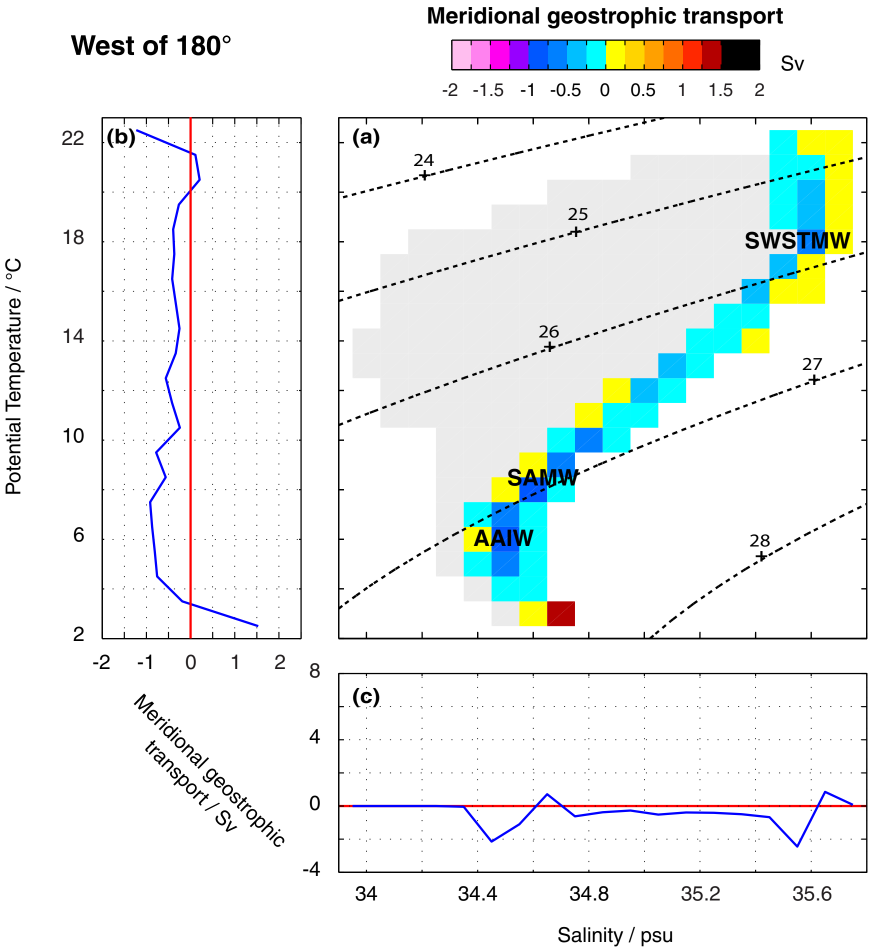

Figure 12. Trajectory-based transport west of 180° at 32°S (a) separated into 1.0°C by 0.1 psu bins, (b) per unit temperature (°C) summed across all salinities, and (c) per 0.1 psu of salinity summed across all temperatures, averaged from 2004 to 2012. Northward transport is positive. The black lines correspond to 2004–2012 mean potential density anomaly contours (kg m^{-3}). In gray is represented the basin-wide transport at 32°S separated into 1.0°C by 0.1 psu bins.

12 month running mean of the SAM index exceeds 0.25. Negative phases of the SAM correspond to a SAM index lower than −0.25. At interannual time scales, the variability of geostrophic transport east of the dateline is about half the variability of the western Pacific (Figure 13b). The interannual anomalies in geostrophic transport east of the dateline appear to exhibit a 2 year periodicity uncorrelated with the SAM. The time variability in the basin-wide geostrophic transport at 32°S resembles the transport in the western Pacific and is characterized by an increase during the positive phases of the SAM and a decrease during the negative phases of the SAM (Figure 13c).

The simultaneous increase in the EAC and EAC recirculation is in agreement with altimetric height time series for the same time period (Figure 14). During the positive phase of the SAM, the altimetric height maxima at the offshore limit of the EAC region indicate a simultaneous strengthening of the geostrophic transport in the EAC and the EAC recirculation. This tendency results from local wind stress curl forcing in the EAC region, which has a positive anomaly during positive SAM phases (Figure 15). This is consistent with

Table 3. Geostrophic Transport for Surface and Mode Waters, SAMW, and AAIW at 32°S

Mode Water	Surface and Mode Waters	SAMW	AAIW
σ_0/kg m^{-3}	<26.5	26.5–27	27–27.3
Transport/Sv	7.3 ± 0.9	4.9 ± 1.0	4.9 ± 1.4

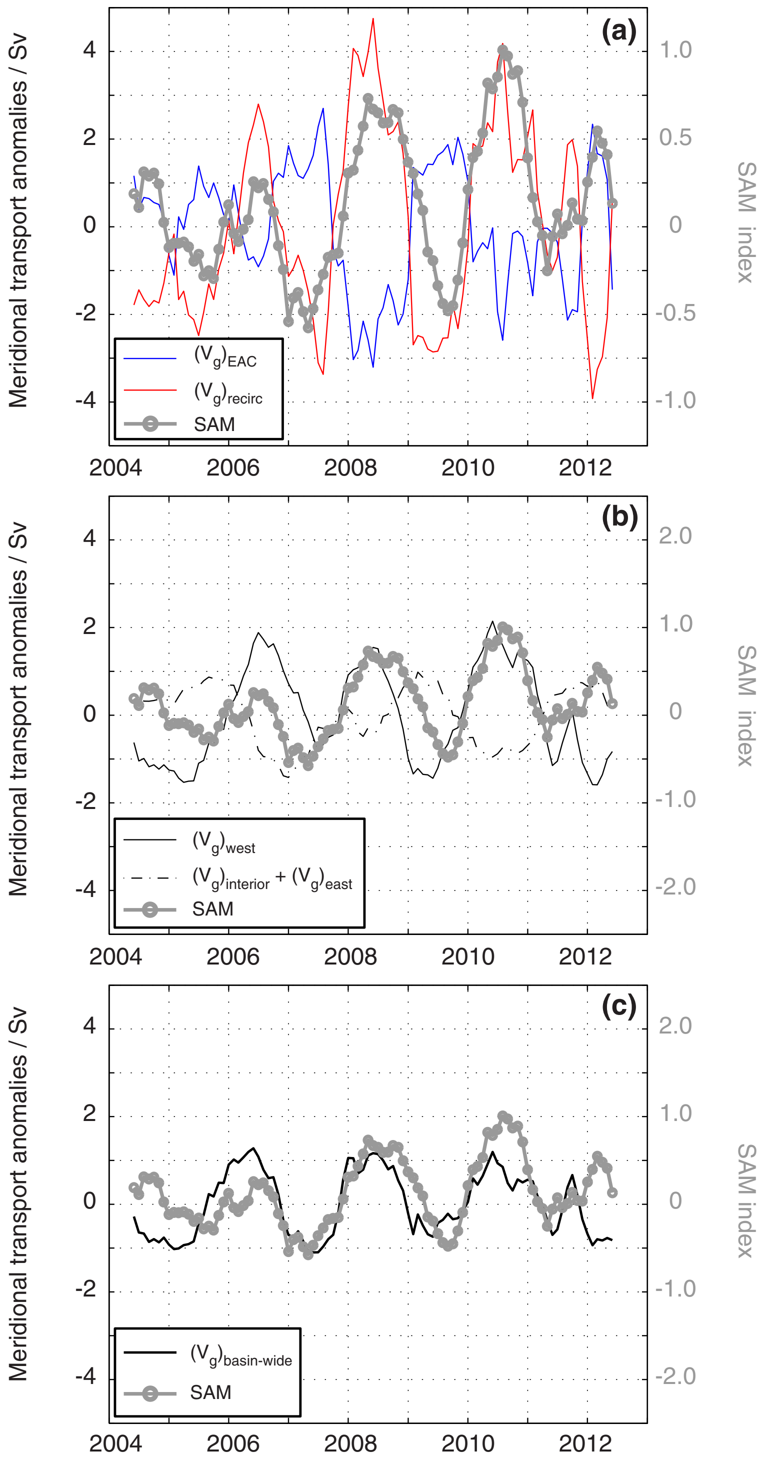

Figure 13. Time series of 0–2000 m geostrophic transport anomaly (a) in the EAC (blue) and in the EAC recirculation region between 154.5°E and 180°E (red), (b) in the western Pacific (continuous line) and east of the dateline (dashed line), and (c) basin-wide at 32°S, versus the SAM index for monthly values from 2004 to 2012.

the observed sea level rise and corresponding spin-up of the EAC and its recirculation (Figures 16a and 16b). The reverse occurs during the negative phase of the SAM.

The interannual anomalies in surface geostrophic transport using Argo at 32°S are similar to AVISO values averaged for 33.5°S–30.5°S (Figures 16a–16c). Regression slopes of AVISO transports at the western

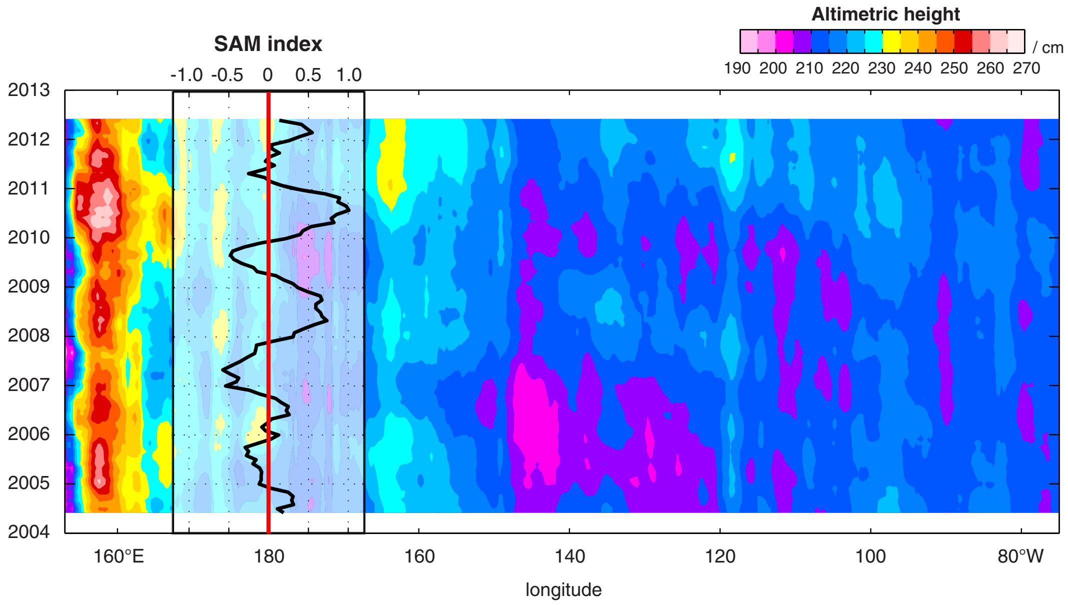

Figure 14. Sea surface height time series estimated as the sum of steric height of the sea surface relative to 2000 m at 32°S, using Argo, plus altimetric height anomaly at 30.5°S–33.5°S from AVISO, for monthly values, 2004 to 2012. (inset) Time series of SAM index.

boundary and in the interior onto the SAM index computed from 2004 to 2012 agree within 95% confidence with estimates from 1993 to 2012 (not shown). The anomalies in surface geostrophic transport using Argo and AVISO indicate a strengthening of the transport in the EAC, EAC recirculation, and in the interior from 2004 to 2012 that coincides with a SAM increase over the same time period. This SAM signature at decadal time scales seen in the EAC transport at the surface is in agreement with the numerical predictions of *Hill et al*. [2010], who showed that the time variability of EAC transport is related to wind stress curl forcing in the subtropical gyre. The decadal trend seen at the surface is not obvious in the 0–2000 m transport anomalies (Figures 13 and 16).

At interannual time scales, the time variability in the basin-wide geostrophic transport at 32°S does not show an obvious ENSO signal (Figure 17a). The Niño 3.4 index used in this work is based on the NOAA Optimal Interpolation Sea Surface Temperature for the 30 year period 1981–2011, 190°E–240°E, 5°S–5°N (http://www.emc.ncep.noaa.gov/research/cmb/sst-analysis/) [*Reynolds et al*., 2002]. From 2004 to 2012, ENSO-related wind stress curl anomalies computed along the eastern coast of Australia at 32°S are weak compared to SAM-related anomalies (not shown). The ENSO signature seen by *Zilberman et al*. [2013] in the

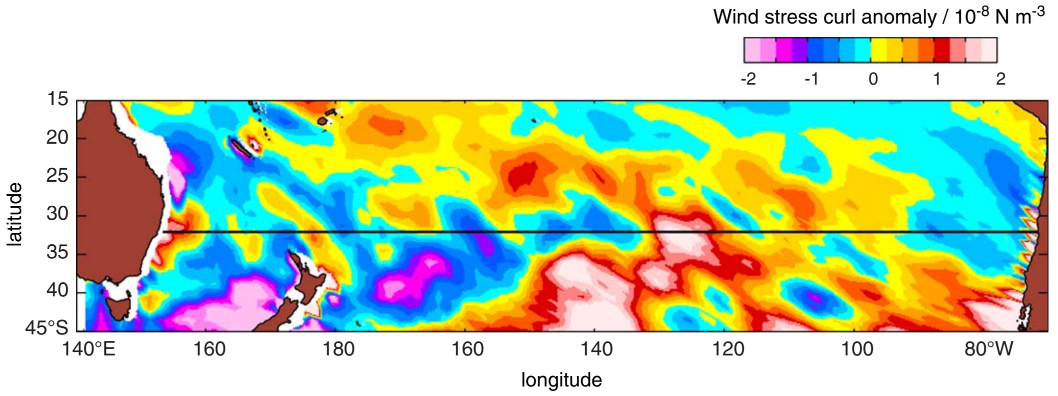

Figure 15. Wind stress curl anomaly averaged over times when the SAM index is greater than 0.25, during 2004–2012. The continuous line indicates 32°S.

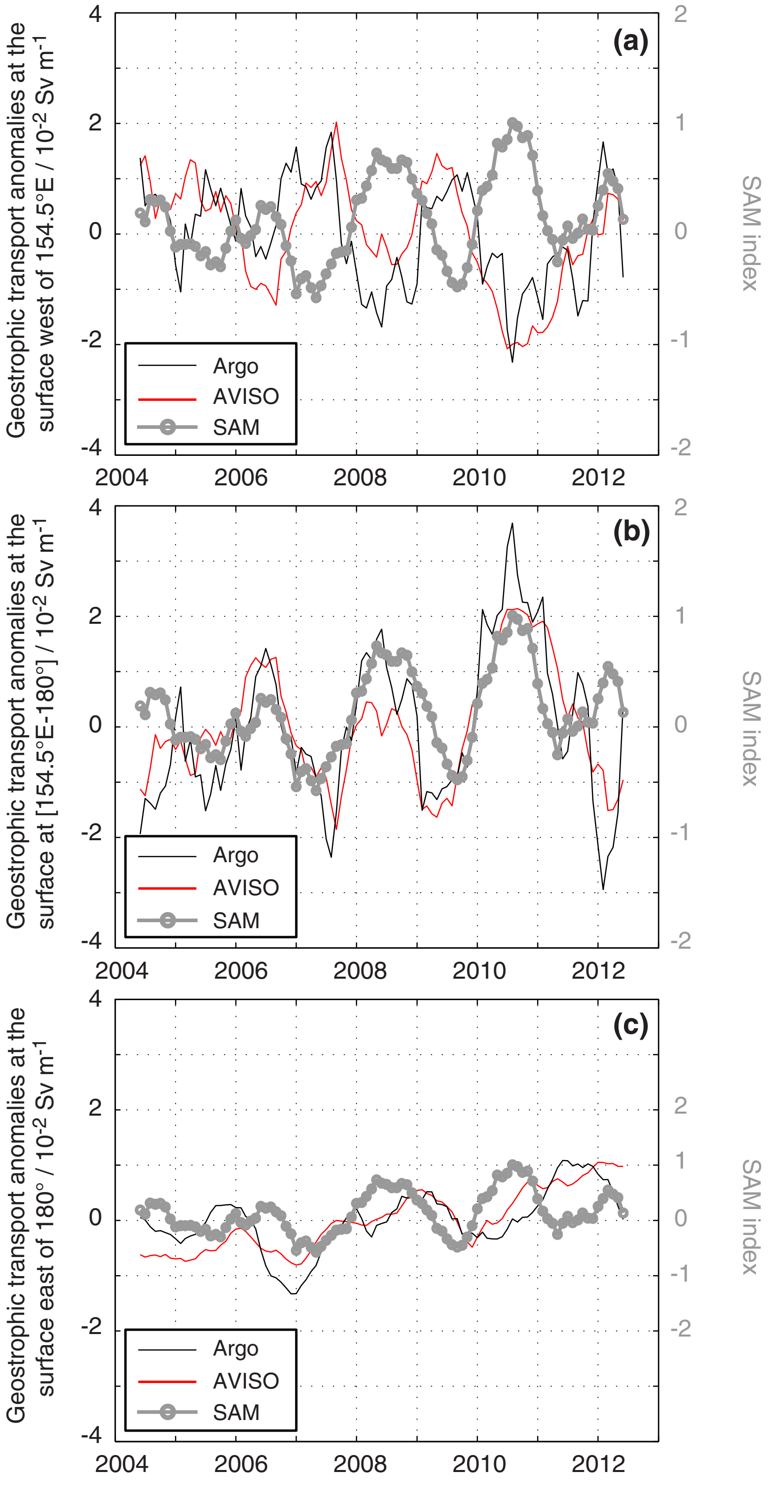

Figure 16. Time series of the geostrophic transport anomaly per unit depth at the sea surface computed using AVISO for 30.5°S–33.5°S (red) and Argo at 32°S (black) west of 154.5°E (a), for 154.5°E–180°E (b), and east of 180° (c) versus the SAM index for monthly values from 2004 to 2012.

basin-wide geostrophic transport anomalies of the shallow MOC at 7.5°S is mostly compensated by storage of warm water layers in the upper 150 m between 7.5°S and 32°S (not shown). Relative to the 2004–2012 mean, the basin-wide Ekman transport anomalies computed using ECMWF and NCEP appear to exhibit a 2

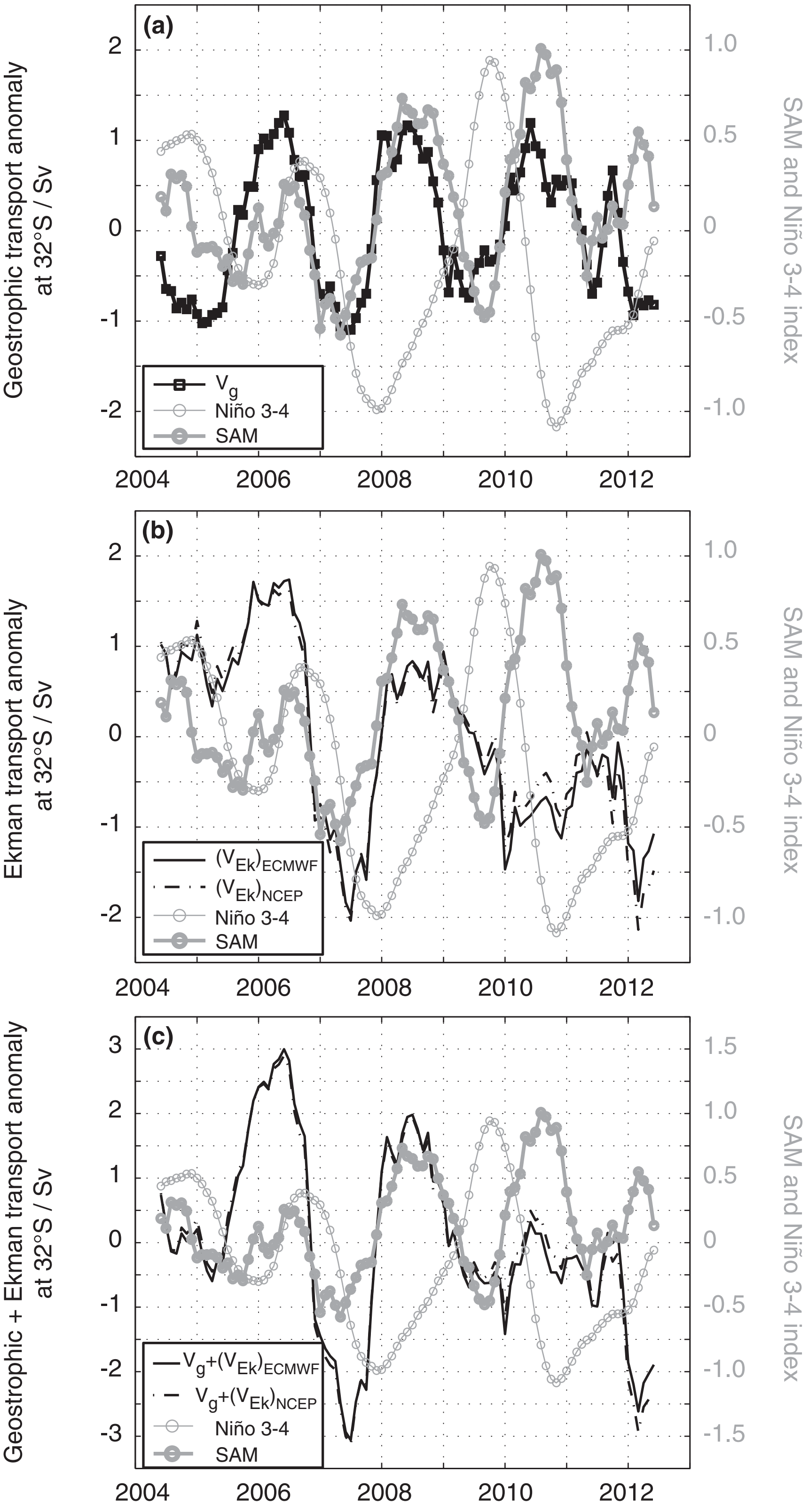

Figure 17. (a) Time series of the geostrophic transport anomalies, (b) Ekman transport anomalies using NCEP and ECMWF, and (c) the geostrophic and Ekman transport residual anomalies using NCEP and ECMWF for the Ekman transport at 32°S versus the Niño 3.4 index and SAM index for monthly values of 2004–2012.

year periodicity rather than a SAM or ENSO correlation (Figure 17b). The anomalies in the residual of V_g and V_{Ek} do not show a clear SAM or ENSO signature (Figure 17c).

4. Summary and Conclusions

The objectives of this study have been twofold: (i) to improve estimates of the mean northward upper ocean transport in the South Pacific at midlatitudes while testing the capabilities of the 9 year Argo profile and trajectory data set and (ii) to investigate the time-variability of the transport for 2004–2012 using Argo, altimetry, and atmospheric reanalysis data.

Our best estimate of the 2004–2012 mean geostrophic transport at 32°S is computed with reference velocity at 1000 m based on Argo trajectories and includes a correction for systematic error generated by vertical shear during the float ascent and descent between surface and parking depth. Random errors generated by the variability and number of trajectory estimates represent the largest source of uncertainty in basin-wide transport. The mean EAC transport estimate of 23.3 ± 2.9 Sv southward is in agreement with *Mata et al*. [2000] and *Wijffels et al*. [2001]. The net mean transport is 20.8 ± 6.0 Sv basin-wide, 10.8 Sv greater than the transport constraint imposed by *Wijffels et al*. [2001]. In the present study, the transport and error are estimated, whereas *Wijffels et al*. [2001] used the ITF transport to constrain the transport at P6 to be 10 ± 5 Sv. As shown in section 3.3, the EAC and recirculation show significant variability at interannual time scales. For this reason, *Wijffels et al*.'s [2001] shear estimate, based on a single trans-Pacific hydrographic section, may be unrepresentative of the time mean. In this study, the ITF was estimated as the residual of the net transport, Bering Strait throughflow, evaporation, precipitation, and vertical transport at 2000 m over all of the Pacific north of 32°S. Our mean ITF estimate of 20.8 ± 6 Sv agrees within error with local observations in the Indonesian Seas. The geostrophic transport maxima at 32°S in the interior and eastern Pacific consist of SAMW and AAIW carried equatorward. The fresh and cool SAMW and AAIW return poleward in the EAC region as saltier and warmer waters. Our 2004–2012 mean transport estimates at 32°S for the SAMW and AAIW layers (Table 3) are consistent with formation rates of water masses inferred from CFC inventories in the South Pacific.

In addition to the mean flow, our analysis focuses on the time variability of the geostrophic transport at 32°S at interannual time scales. Changes in basin-wide transport are dominated by transport anomalies in the western boundary current region. The simultaneous increase of the EAC and the EAC recirculation during the positive phase of the SAM and simultaneous decrease during the negative phase are linked to changes in the wind stress curl tied to the SAM. No evident ENSO signature was found in the geostrophic transport variability at 32°S at interannual time scales. Uncertainties remain in the time-varying transport of the EAC due to a lack of Argo profiles. Ongoing high-resolution expendable bathythermograph sampling combined with additional Argo float deployments will help assess the time-variability of the EAC and its recirculation.

Acknowledgments
The Argo data used here were collected and are made freely available by the International Argo Program and by the national programs that contribute to it. The authors thank John Gilson, Megan Scanderbeg, and Lisa Lehmann for valuable suggestions. This work was supported by U.S. Argo through NOAA grant NA10OAR4310139 (SIO CIMEC Argo) and NASA grant NNX13AE82G. The altimeter products were provided by AVISO with support from the Centre National d'Etudes Spatiales (CNES).

References

Berrisford, P., D. Dee, K. Fielding, M. Fuentes, P. Kallberg, S. Kobayashi, and S. Uppala (2009), The ERA-Interim archive, version 1.0, *Tech. Rep*., Eur. Cent. for Medium Range Weather Forecasts. Shinfield Park, Reading, Berkshire, U. K.

Cai, W. (2006), Antarctic ozone depletion causes an intensification of the Southern Ocean super-gyre circulation, *Geophys. Res. Lett*., *33*, L03712, doi:10.1029/2005GL024911.

Coachman, L. K., and K. Aagaard (1998), Transports through Bering Strait: Annual and interannual variability, *J. Geophys. Res*., *93*(C12), 15,535–15,539.

Cornuelle, B., and D. Roemmich (1992), The subtropical mode waters of the South Pacific Ocean, *J. Phys. Oceanogr*., *22*, 1178–1187.

Emery, W. J. (2001), *Water Types and Water Masses in Encyclopedia of Ocean Sciences*, edited by J. Steele, pp. 1556–1567, Academic, San Diego, Calif.

Ganachaud, A., and C. Wunsch (2003), Large-scale ocean heat and freshwater transports during the World Ocean Circulation Experiment, *J. Clim*., *16*, 696–705.

Grist, J. P., and S. A. Josey (2003), Inverse analysis adjustment of the SOC air-sea flux climatology using ocean heat transport constraints, *J. Clim*., *16*, 3274–3295.

Hanawa, K., and L. D. Talley (2001), Mode waters, *in Ocean Circulation and Climate*, edited by G. Siedler, J. Church, and J. Gould, pp. 373–386, Academic, San Diego, Calif.

Hartin, C. A., R. A. Fine, B. M. Sloyan, L. D. Talley, T. K. Chereskin, and J. Happel (2011), Formation rates of Subantarctic mode water and Antarctic intermediate water within the South Pacific, *Deep Sea Res., Part I*, *58*, 524–534.

Hill, K. L., S. R. Rintoul, R. Coleman, and K. R. Ridgway (2008), Wind forced low frequency variability of the East Australia Current, *Geophys. Res. Lett*., *35*, L08602, doi:10.1029/2007GL032912.

Hill, K. L., S. R. Rintoul, P. R. Oke, and K. R. Ridgway (2010), Rapid response of the East Australian Current to remote wind forcing: The role of barotropic-baroclinic interactions, *J. Mar. Res.*, *68*, 413–431.

Jackett, D., and T. McDougall (1997), A neutral density variable for the world's oceans, *J. Phys. Oceanogr.*, *27*, 237–263.

Kalnay, E., et al. (1996), The NCEP/NCAR 40-year reanalysis project, *Bull. Am. Meteorol. Soc.*, *77*, 437–471.

Karstensen, J. (2004), Formation of the South Pacific shallow salinity minimum: A Southern Ocean pathway to the tropical Pacific, *J. Phys. Oceanogr.*, *34*, 2398–2412.

Lee, T., and I. Fukumori (2003), Interannual-to-decadal variations of tropical-subtropical exchange in the Pacific Ocean: Boundary versus interior pycnocline transports, *J. Phys. Oceanogr.*, *16*, 4022–4042.

Macdonald, A. M., S. Mecking, P. E. Robbins, J. M. Toole, G. C. Johnson, L. Talley, M. Cook, and S. E. Wijffels (2009), The WOCE-era 3-D Pacific Ocean circulation and heat budget, *Prog. Oceanogr.*, *82*, 281–325.

Mata, M. M., M. Tomczak, S. Wijffels, and J. A. Church (2000), East Australian Current volume transports at 30°S: Estimates from the World Ocean Circulation Experiment hydrographic sections PR11/P6 and the PCM3 current meter array, *J. Geophys. Res.*, *105*(C12), 28,509–28,526.

McCartney, M. S. (1977), A voyage of discovery, *Deep Sea Res.*, *24*(Suppl.), 103–119.

McDougall, T. J., and A. Klocker (2010), An approximate geostrophic streamfunction for use in density surfaces, *Ocean Modell.*, *32*, 105–117.

Mo, K. C. (2000), Relationships between low-frequency variability in the southern hemisphere and sea surface temperature anomalies, *J. Clim.*, *13*, 3599–3610.

Montes, I., F. Colas, X. Capet, and W. Schneider (2010), On the pathways of the equatorial subsurface currents in the eastern equatorial Pacific and their contributions to the Peru-Chile Undercurrent, *J. Geophys. Res.*, *115*, C09003, doi:10.1029/2009JC005710.

Munk, W. H., and C. Wunsch (1998), Abyssal recipes II: Energetics of tidal and wind mixing, *Deep Sea Res., Part I*, *45*, 1977–2010.

Park, J., K. Kim, B. King, and S. Riser (2005), An advanced method to estimate deep currents from profiling floats, *J. Atmos. Oceanic Technol.*, *22*, 1294–1304.

Reid, J. L. (1973), Transpacific hydrographic sections at Lats. 43°s and 28°s: The SCORPIO expedition III. Upper water and a note on southward flow at mid-depth, *Deep Sea Res. Oceanogr. Abstr.*, *20*, 39–49.

Reynolds, R. W., N. A. Rayner, T. M. Smith, D. C. Stokes, and W. Wang (2002), An improved in situ and satellite SST analysis for climate, *J. Clim.*, *15*, 1609–1625.

Ridgway, K. R., and J. R. Dunn (2003), Mesoscale structure of the mean East Australian Current system and its relationship with topography, *Prog. Oceanogr.*, *56*, 189–222.

Roemmich, D. H., J. Gilson, R. Davis, P. Sutton, S. Wijffels, and S. Riser (2007), Decadal spinup of the South Pacific subtropical gyre, *J. Phys. Oceanogr.*, *37*, 162–173.

Sato, K., and T. Suga (2009), Structure and modification of the South Pacific Eastern Subtropical Mode Water, *J. Phys. Oceanogr.*, *39*, 1700–1714.

Schneider, W., R. Fuenzalida, E. Rodríguez-Rubio, and J. Garcés-Vargas (2003), Characteristics and formation of Eastern South Pacific Intermediate Water, *J. Geophys. Res.*, *30*(11), 1581, doi:10.1029/2003GL017086.

Shaffer, G., S. Hormazabal, O. Pizarro, and S. Salinas (1999), Seasonal and interannual variability of currents and temperature off central Chile, *J. Geophys. Res.*, *104*(C12), 29,951–29,961.

Sprintall, J., S. E. Wijffels, R. Molcard, and I. Jaya (2009), Direct estimates of the Indonesian Throughflow entering the Indian Ocean: 2004–2006, *J. Geophys. Res.*, *114*, C07001, doi:10.1029/2008JC005257.

Talley, L. D. (2003), Shallow, intermediate, and deep overturning components of the global heat budget, *J. Phys. Oceanogr.*, *33*, 530–560.

Talley, L. D. (2008), Freshwater transport estimates and the global overturning circulation: Shallow, deep, and throughflow components, *Prog. Oceanogr.*, *78*, 257–303.

Thompson, D. W. J., and J. M. Wallace (2000), Annular modes in the extratropical circulation. Part I: Month-to-month variability, *J. Clim.*, *13*, 1000–1016.

Tilburg, C. E., H. E. Hurlburt, J. J. O'Brien, and J. F. Shriver (2001), The dynamics of the East Australian Current system: The Tasman Front, the East Auckland Current, and the East Cape Current, *J. Phys. Oceanogr.*, *31*, 2917–2943.

Tomczak, M. (2006), Variability of Antarctic intermediate water properties in the South Pacific Ocean, *Ocean Sci.*, *3*, 2021–2058.

Tsuchiya, M. (1998), A Pacific hydrographic section at 88°W: Water-property distribution, *J. Geophys. Res.*, *103*(C6), 12,899–12,918.

Wijffels, S. E., J. M. Toole, and R. Davis (2001), Revisiting the South Pacific subtropical circulation: A synthesis of World Ocean Circulation Experiment observations along 32°S, *J. Geophys. Res.*, *106*(C9), 19,481–19,513.

Wong, A. P. S., and G. C. Johnson (2003), South Pacific Eastern Subtropical Mode Water, *J. Phys. Oceanogr.*, *33*, 1493–1509.

Wunsch, C., and P. Heimbach (2007), Practical global oceanic state estimation, *Physica D*, *230*, 197–208.

Zilberman, N. V., D. H. Roemmich, and S. T. Gille (2013), The mean and the time-variability of the shallow meridional overturning circulation in the tropical South Pacific Ocean, *J. Clim.*, *26*, 4069–4087.